

Unlocking Electro-optic Resonant Phase Shifting for Multi-dimensional, Ultra-dynamic Photonic Switches

Lingzhi Luo, Rui Ma, Richard V. Penty, *Senior Member, IEEE* and Qixiang Cheng

Abstract—Optical circuit switching is connection-oriented, being deterministic through the reservation of a complete wavelength channel or spatial path for a certain period. However, this comes at a trade-off against link dynamics, and overall capacity can thus be constrained by the time slot reservations, especially for switches with microsecond- to millisecond-scale reconfiguration times. For data-intensive applications, the communication patterns associated with random data sets typically yield short-lived flows. This situation calls for a new multi-dimensional switching paradigm that fully exploits not only the space and wavelength domains but also with nanosecond-scale reconfigurable capability in the time domain to enable ultra-dynamic links. In this work, we focus on the exploitation of micro-ring resonant phase shifters (RPSs) that are wavelength selective for optical switching in a single plane. By proposing an innovative analytical method with transmission circle chart, we fully unlock the power of RPS with nanosecond-scale reconfigurability and the capability to arbitrarily manipulate its phase and amplitude. Such a compact model offers fresh insights into designs with under and critically coupled RPSs beyond the commonly explored over-coupling condition. This creates not only versatile switch elements but also perfect absorbers for robust multi-wavelength operations. The proposed device can bring about a breakthrough in the optical switching capacity that potentially addresses the challenges faced by modern data center networks, as well as other photonic circuits for high-throughput signal processing.

Index Terms— Micro-ring resonators, phase shifters, optical switches and optical phase shifters

I. INTRODUCTION

THE increasing demands for emerging high-volume and latency-constrained applications, such as artificial intelligence (AI), autonomous vehicles (AV), and augmented/virtual reality (AR/VR), are imposing stringent requirements on data center network capacity, latency, energy consumption, and guaranteed delivery[1], [2]. Current data center interconnects using static node configurations are being

^Manuscript received XXXX XX, XXXX; revised XXXX XX, XXXX; accepted XXXX XX, XXXX. This work was supported by European Union’s Horizon Europe Research and Innovation Program under Agreement 101070560 (PUNCH).

The authors are with the Centre for Photonic Systems, Electrical Engineering Division, Department of Engineering, University of Cambridge, Cambridge, CB3 0FA, U.K. (e-mail: ll672@cam.ac.uk, rm2126@cam.ac.uk, rvp11@cam.ac.uk, and qc223@cam.ac.uk).

Color versions of one or more of the figures in this paper are available online at <http://ieeexplore.ieee.org>. Digital Object Identifier

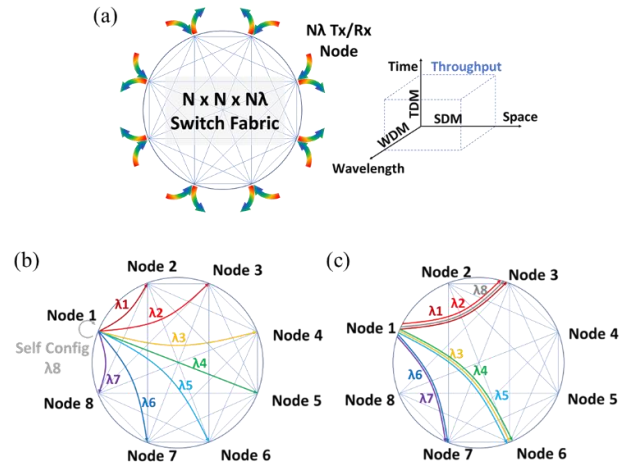


Fig. 1. (a) Conceptual figure of a fully non-blocking $N \times N \times N$ λ optical switch fabric. (b) All-to-all reconfigurable interconnection by allocating a wavelength to any pair of nodes. (c) Bandwidth steering by grouping multiple wavelengths between hot nodes.

pushed to their limits by the diverse demands of this set of applications. Flexible architectures that match their capacity to an application’s traffic pattern can deliver optimized connectivity while eliminating over-provisioned resources[3]. Transparent optical switches are the key enablers.

Mass-manufacturable photonic integration technologies are favorable for data centers, where cost-effectiveness is a primary concern [4]. Thousands of photonic components have been integrated onto a single chip for large-scale switch fabrics [5], [6]. These demonstrations are broadband and capable of handling wavelength division multiplexing (WDM) data for modulation-agnostic switching, but only reconfigurability in the space domain has been exploited for coarse routing. Switching at the wavelength granularity, which allows for finer-level information access, is becoming vital as short-reach interconnects approach petabit/s-scale capacity with massively parallel wavelength channels [7]. Apart from the fact that only few explorations have been made of chip-scale space-and-wavelength switches, designs often adhere to parallel space switching planes, bookended by wavelength (de)-multiplexers [8], posing immense challenges to the complexity of photonic integrations. In contrast, space-and-wavelength switching can be realized using wavelength-selective elementary switch cells, such as add-drop micro-ring resonators (MRRs) [9], [10] in a tailored topology.

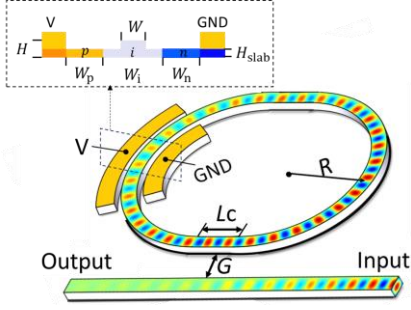


Fig. 2. Schematic diagrams of Electro-optical RPS. R: radius of the bend waveguide, Lc: the length of straight coupling waveguide, G: the gap between the straight coupling waveguide and the bus waveguide., W: waveguide width. H: waveguide height, H_{slab} :slab thickness. Wp, Wi, Wn: width of p zone, intrinsic zone and n zone.

These critically-coupled MRR filters are often susceptible to fabrication variations and still worse, to electro-absorption losses. This leaves little room for E-O MRR switch fabrics and indeed, this type of device has been sparsely reported [11]. Figure 1(a) illustrates a conceptual figure of a multi-dimensional switch that can break the trade-off between flexibility and determinism by offering reconfigurable interconnects from all-to-all links, as shown in Fig. 1(b), to imbalanced group-to-group traffic by bandwidth steering, as shown in Fig. 1(c). A space-and-wavelength switch fabric forms the core for arbitrarily routing any combination of wavelengths from any input to any output. An extra key lies in the ultra-fast reconfigurability, which is a cornerstone that enables unparalleled dynamics by multiplexing in the time domain. Prior studies used MRRs to build space-and-wavelength switches[12], [13]; however, the stringent management on fabrication variations poses a challenge. An alternative approach utilized over-coupled MRRs as phase shifters but with transmission asymmetry and/or high insertion loss[14], [15], [16].

In this paper, by proposing a powerful and innovative analytical method with transmission circle chart, we fully unlock the power of RPS with electro-optic (E-O) nanosecond-scale reconfigurability. Manipulation of the coupling strength, which is the key to tweaking its performance, can be simply done by adjusting the position of points on the transmission circle chart and altering the circle shape. We extend the model beyond the commonly utilized over-coupling regime to explore under and critically coupled conditions and outline their role, creating both versatile multi-wavelength switch elements and perfect absorbers. As a benchmark, our exploration in the design of RPS confirms its superiority over conventional add-drop MRRs. This presents as an efficient design methodology for the tailoring of RPS elements, potentially bringing about a breakthrough in the field of optical switching and signal processing.

II. TRANSMISSION CIRCLE CHART OF RPS

MRRs exhibit a strong resonance phenomenon, wherein even slight deviation from the resonance results in a significant phase change. This character can be harnessed for efficient narrow-band phase manipulation, which forms RPSs. Figure 2 illustrates the structure of a racetrack E-O RPS with key

geometric parameters. Their optical field transmission coefficient (t_{MRR}) can be expressed as [17]:

$$t_{MRR}(\phi) = e^{i(\pi+\phi)} \frac{a - re^{-i\phi}}{1 - ra e^{i\phi}} \quad (1)$$

where a and r are the single-pass amplitude transmission coefficient and the self-coupling coefficient, respectively. $\phi = \beta L$ is the single-pass phase shift, with L as the round-trip length and β as the propagation constant. The argument and the square of modulus of t_{MRR} are defined as the effective phase shift (φ) and power transmission coefficient (T), respectively, which can be given as:

$$\varphi(\phi) = \pi + \phi + \arctan\left(\frac{r \sin(\phi)}{a - r \cos(\phi)}\right) + \arctan\left(\frac{ra \sin(\phi)}{1 - r a \cos(\phi)}\right), a > r \quad (2)$$

$$\varphi(\phi) = -\arctan\left(\frac{a \sin(\phi)}{r - a \cos(\phi)}\right) + \arctan\left(\frac{ar \sin(\phi)}{1 - ar \cos(\phi)}\right), a \leq r$$

$$T(\phi) = |t_{MRR}(\phi)|^2 = \frac{a^2 - 2r a \cos \phi + r^2}{1 - 2ar \cos \phi + (ra)^2} \quad (3)$$

To precisely describe the behavior of the RPS, it is crucial to understand the loss incurred during arbitrary phase shifting. Thus, to ascertain the correlation between $\varphi(\phi)$ and $|t_{MRR}(\phi)|$, we decompose t_{MRR} into its real and imaginary components (x, iy) and plot them on the complex plane with varying ϕ . Consequently, with ϕ increasing, t_{MRR} rotates counterclockwise and finally traces out a circular locus that satisfies the equation below:

$$\left(x - \frac{(a^2 - 1)r}{a^2 r^2 - 1}\right)^2 + y^2 = \left(\frac{a(r^2 - 1)}{a^2 r^2 - 1}\right)^2 \quad (4)$$

This creates a transmission circle chart that is centered at $\alpha = ((a^2 - 1)r/(a^2 r^2 - 1), 0)$ with a radius of $R_c = a(r^2 - 1)/(a^2 r^2 - 1)$. The angle and magnitude of vectors from the origin (point O) to a specific point on the circle correspond to $\varphi(\phi)$ and $|t_{MRR}(\phi)|$, respectively. Vector OA that points from O to the leftmost point on the circle corresponds to $t_{MRR}(\phi)$ at resonance. Based on the relative values of a and r , the transmission circle chart can be divided into 3 cases that are illustrated by Fig. 3(a)-(c), respectively. (I) When $a < r$, the RPS is in the under-coupled regime and O is outside the circle. Therefore, there are two extremums ($\pm\theta_m$) on the effective phase shift curve as shown in Fig. 3(d), corresponding to the vectors OB and OC that are tangent to the circle in Fig. 3(a). (II) When $a = r$, the RPS is critically coupled, and O is on the circle so the transmission is zero. When the ring deviates from resonance by a plus or minus infinitesimal value, the angle of the corresponding vector undergoes an abrupt transition to $\pm\pi/2$. This accounts for the phase jump observed in Fig. 3(e). (III) When $a > r$, the RPS is in the over-coupled regime and O is inside the circle so the angle of the vector from O to the point on the circle can take all values from 0 to 2π continuously, as shown in Fig. 3(f). When

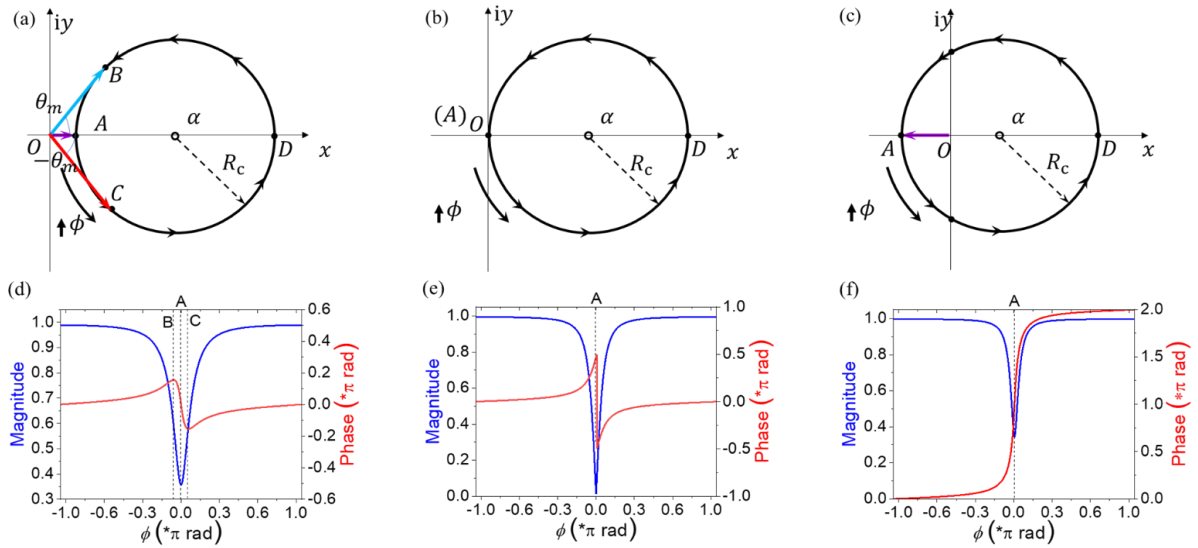


Fig. 3. Transmission circle chart when RPS in (a) under-coupled regime, (b) critical-coupled regime and (c) over-coupled regime. Vector OA corresponds to t_{MRR} in resonance. Vectors OB and OC are tangent to the under-coupled transmission circle chart with phase extremums of θ_m and $-\theta_m$ respectively. Magnitude transmission and effective phase shift curves when RPS in (d) under-coupled regime, (e) critical-coupled regime and (f) over-coupled regime. Point A, B and C correspond to the vector OA, OB and OC in Fig. 3 (a)-(c).

the RPS is implemented with thermo-optic (T-O) phase controllers, i.e., heaters, a remains constant and so analyses can be conducted in a single transmission circle chart with a fixed center of circle and radius. As for E-O phase controllers, i.e., by carrier injections, a would vary due to induced electro-absorption losses at different carrier concentrations. Consequently, each point of t_{MRR} corresponds to a distinct transmission circle chart, as depicted in Fig. 4(a). As a decreases, α shifts to the right along the x -axis, and R_c decreases. The transformation for the transmission circles of E-O RPS can be expressed as:

$$\begin{cases} x = \frac{(a^2 - 1)r}{a^2r^2 - 1} + \frac{a(r^2 - 1)}{a^2r^2 - 1} \cos \varphi(\phi) \\ y = \frac{a(r^2 - 1)}{a^2r^2 - 1} \sin \varphi(\phi) \end{cases} \quad (5)$$

Here, a is not constant but varies depending on several factors, including doping levels (N), bias voltages (V), and the RPS structure. Consequently, in accordance with equation (2), the value of φ will change corresponding to variations in a . The specific details regarding the dependencies of a and φ are available in APPENDIX A. Figure 4(b) illustrates the distorted transmission circle of an E-O RPS according to APPENDIX A.

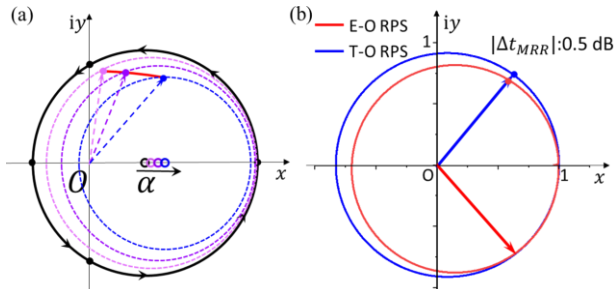


Fig. 4. (a) Schematic diagrams for distorted transmission circle trajectory formation of an EO MRPS. (b) The distorted transmission circles of T-O and E-O RPS

It shows that when a large phase shift is induced, the transmission phase and magnitude closely resemble the original non-loss transmission circle. As depicted in Fig. 4(b), the maximum transmission difference Δt_{MRR} corresponds to a merely insertion loss increase of ~ 0.5 dB at $3\pi/4$ phase shift.

III. RPS BASED SWITCHING ELEMENTS

A. Over-coupled RPSs

As illustrated in Fig. 5(a), leveraging their narrow-band frequency response, multiple pairs of RPSs can be embedded in the two arms of a balanced MZI. These RPSs are tailored to operate in the over-coupled regime, in order to provide a continuous phase response ranging from 0 to 2π near resonance.

Starting with the most basic case, in which a single pair of RPS (RPS1 and RPS1') is utilized. To tackle asymmetrical transmission response between the bar and the cross state, a $\pi/2$ wideband phase change is introduced to convert the even symmetry transmission of MZI into odd symmetry. In this case, switching from the bar to the cross state can be accomplished by blueshifting the resonance wavelength of RPS1 to λ_{0b} , leading to a $3\pi/4$ phase advance at the operating wavelength (λ_0) in the lower arm, and redshifting the resonance wavelength of RPS1' to λ_{0r} , resulting in a $3\pi/4$ phase delay in the upper arm. Consequently, the RPS-induced phase difference amounts to $3\pi/2$. With an additional phase bias of $\pi/2$, the phase difference ($\Delta\varphi$) becomes 2π , allowing for switching from the bar to the cross, as illustrated in Fig. 5(b). Conversely, interchanging the operation on RPS1 and RPS1', the RPS-induced phase difference becomes $-3\pi/2$. Adding an extra $\pi/2$ phase bias leads to $\Delta\varphi = -\pi$, enabling switch from the cross to the bar. This push-pull control scheme effectively enables symmetrical switching, as depicted in Fig. 5(c).

Since symmetrical transmission between the bar and cross

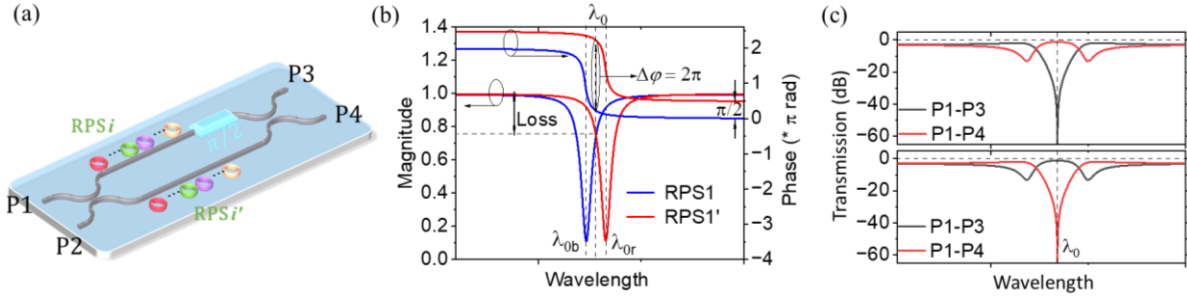


Fig. 5. (a) Schematic of an MZI with multiple pairs of RPS. (b) Power transmission and phase delay of RPS 1 and RPS1' in cross state under $\pi/2$ phase bias configuration. (c) Power transmission of an MZI with single pair of RPSs in bar state and cross state under $\pi/2$ phase bias configuration.

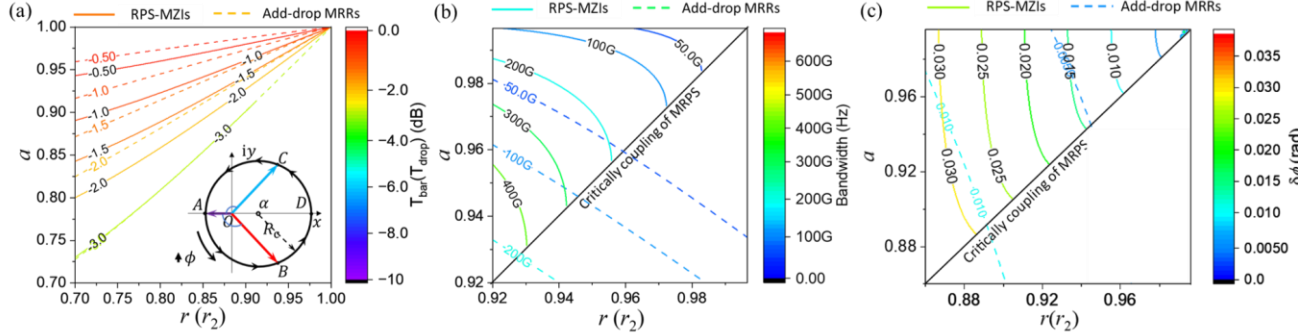


Fig. 6. (a) T_{bar} Contours of RPS-MZIs in different a and r under $\pi/2$ phase bias configuration (solid lines). T_{drop} Contours of critically add-drop MRRs in different a and self-coupling coefficient (r_2) (dashed lines). Inset: over coupled RPS transmission circle chart under $\pi/2$ phase bias configuration. (b) Bandwidth contours of RPS-MZIs in different a and r under $\pi/2$ phase bias configuration (solid lines) and critically add-drop MRRs in different a and r_2 (dashed lines). (c) Phase shift error ($\delta\phi$) contours of RPS-MZIs in different a and r under $\pi/2$ phase bias configuration (solid lines) and critically add-drop MRRs in different a and r_2 (dashed lines).

state is created, their power transmission (T_{bar} , T_{cross}) can be treated equally, and the transmission circle chart is given in the inset of Fig. 6(a). In the T-O tuning case, Vector OB and OC, which have a phase delay of $3\pi/4$ and a phase advance of $3\pi/4$ compared to OA, respectively, correspond to t_{MRR} when the resonance wavelength of RPS1 redshifts to λ_{or} and the resonance wavelength of RPS1 blueshifts to λ_{ob} . The magnitude of OB and OC are the same and T_{bar} and T_{cross} can be obtained simply through its geometry:

$$T_{cross} = T_{bar} = (|OB| + |OC|)^2 / 4 \quad (6)$$

Detailed derivation of (6) and the corresponding resonance wavelength shifts ($\Delta\lambda_{or}$, $\Delta\lambda_{ob}$) can be found in APPENDIX B. Contours of T_{bar} in different a and r are also given in Fig. 6(a) (solid lines). Compared with the insertion loss of add-drop MRRs (dashed lines) that are at critical coupling, the proposed switching element (SE) exhibits an improved insertion loss under the same coupling and single-pass loss conditions. This is attributed to that the operating point of RPSs deviate from its resonance wavelength at a distance of $\Delta\lambda_{or}$.

For a precise analysis of the insertion loss in E-O RPSs, the variation of a has to be taken into consideration. According to Section II and APPENDIX A., for a specific RPS where R and N are determined, analyzing the impact of changes in a during switching hinges on pinpointing the distorted transmission circle chart, specifically identifying the $a(R, V, N)$ when ϕ is $3\pi/4$ and $-3\pi/4$, respectively. Although (6) remains valid, $|OB|$ and $|OC|$ are no longer equal. Instead, different values of a

corresponding to the $3\pi/4$ and $-3\pi/4$ phase shifts have to be used, as elucidated in APPENDIX B.

Unlike the change of ϕ caused by plasma dispersion effect, the ϕ alteration resulting from shifts in the operating wavelength does not induce a variation in a . Therefore, its full width at half maximum (FWHM) and corresponding 3dB-bandwidth (BW) can be given as follows according to APPENDIX C:

$$FWHM(a, r) = \frac{\lambda_0^2 \Delta P_{1/2}(a, r)}{\pi n_g L} \quad (7)$$

$$BW(a, r) = \frac{c}{\lambda_0^2} FWHM(a, r) = \frac{c \cdot \Delta P_{1/2}(a, r)}{\pi n_g L} \quad (8)$$

where $\Delta P_{1/2}$ is the single pass phase shift when the power transmission declines to the half of its peak value, which can be fitted well with a quadric surface given in APPENDIX C. c is the speed of light. Contours of BW in different a and r are also given in Fig. 6(b) (solid lines). Compared to that of critically-coupled add-drop MRRs, the RPS-SEs demonstrate 3-4 times broadened BW under identical coupling and single-pass loss conditions. The BW broadening is especially pronounced under conditions of stronger coupling and higher single-pass loss. Such expanded bandwidth results from the relatively gradual phase change at the $\pm 3\pi/4$ operating point of the MRPSs.

The RPSs operate in the over-coupled regime and are detuned from the resonance point, implying that they should offer enhanced robustness and require lower driving resolution. The contours of the single pass phase shift error due to finite voltage

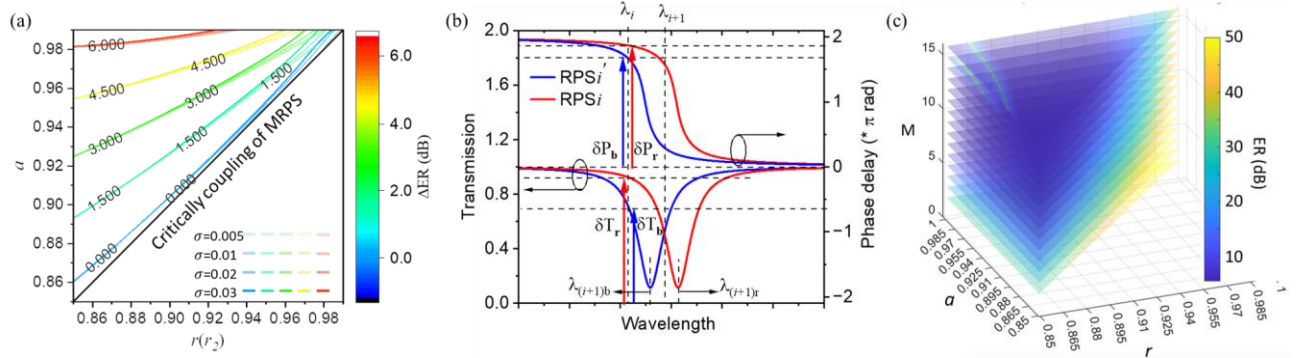


Fig. 7. (a) Expected extinction ratio difference contours (ΔER) of RPS-MZIs over critically add-drop MRRs in different a and $r(r_2)$ under various standard deviation (σ). (b) Schematic diagram of crosstalk from adjacent channels. (c) 3D visualization of the ER for equally spaced channels across varying a , r , and M .

resolution ($\delta\phi$) in different a and r for the RPS-MZIs are given in Fig. 6(c) (solid lines) according to APPENDIX D. These contours correspond to ERs declining to 30 dB due to the single-pass phase error. The required single pass phase tuning resolution (ϕ_{res}) is only one third of that of an add-drop MRR (dashed lines). For random errors like fabrication variations and thermal fluctuations, it can be assumed that $\delta\phi$ follows a normal distribution $N(0, \sigma^2)$. The stability can be characterized by the expected value of ER ($E(ER)$) within the range of 3σ deviation from the mean. Figure 7(a) provides a quantitative comparison. ΔER is defined as the $E(ER)$ difference of the RPS-MZIs over the add-drop rings. This figure indicates that $E(ER)$ values are roughly equivalent in regions near critical coupling. But in regions of over-coupling, as the difference between a and r grows, the $E(ER)$ of the RPS-SE surpasses that of the add-drop rings, indicating enhanced stability. This superiority can be maintained across various variances, as shown in Fig. 7(a).

To ensure optimal performance of multi-wavelength switching with multiple pairs of RPSs, two additional criteria are: 1) the FSR of the RPSs should be large enough to accommodate all wavelength channels; 2) FWHM of the passband of SEs should be narrow enough to minimize crosstalk from adjacent wavelength channels. The first term can be expressed as:

$$\text{Max}\{FSR_i = \frac{\lambda_i^2}{n_g \cdot L}\} \geq \Gamma + \Delta\lambda \quad (9)$$

where Γ is the total band span, and FSR_i and λ_i are the FSR of RPSs and the center operating wavelength of channel i ,

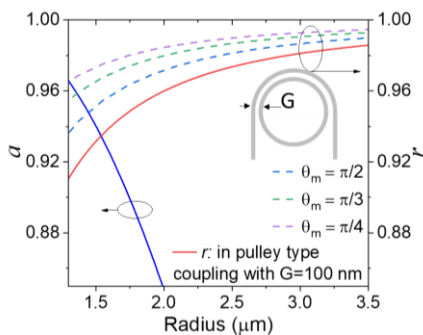


Fig. 8. a (blue line) and r (red line) in different radii of MRRs using pulley type coupling. The dashed lines are the upper limits of r in under-coupled regime for different phase change range.

respectively.

With respect to the second criterion, crosstalk from adjacent wavelength channels will lead to passband peak drift, reduced ER and additional insertion loss. To assess the impact of crosstalk, ER has been selected as the metric. According to APPENDIX E, the deterioration of ER is caused by the unbalanced ratio (α) and the deviation of $\Delta\phi$ from $-\pi$. Here, as illustrated in Fig. 7(b), the channel $i+1$ will introduce different transmission power crosstalk ($\delta T_r, \delta T_b$) and phase crosstalk ($\delta P_r, \delta P_b$) on channel i due to the different resonance wavelength of RPS $i+1$ and RPS $i+1'$. ($\delta P_r, \delta P_b$) and ($\delta T_r, \delta T_b$) are both determined by channel spacing $\Delta\lambda$ and the FWHM, as detailed in APPENDIX E. Therefore, achieving the desired ER requires meticulous control of the $\Delta\lambda$ and the FWHM. Considering crosstalk from all the other channels, the ER for channel i ($ER_i(\alpha_i, \Delta\phi_i)$) can be calculated using transfer function method according to APPENDIX E. Three-dimensional visualization of the ER for equally spaced channels across varying a , r , and M are given in Fig. 7(c). There is a noticeable transition to higher ER as we move upward and diagonally across the plot which indicates that when we increase the channel numbers, a lower single-pass loss and less coupling intensity are required to reduce crosstalk and obtain higher ER.

B. Under-coupled RPSs

In cases where Γ covers a wide spectral range, RPSs with larger FSR become essential. This requirement implies a smaller R , which presents a significant challenge in achieving

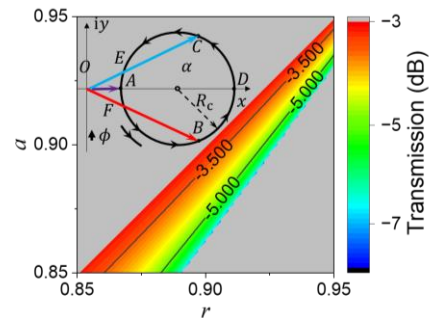


Fig. 9. Contours of T_{bar} (T_{cross}) in different a and r under $\pi/2$ phase bias configuration. Inset: under coupled transmission circle chart under $\pi/2$ phase bias configuration.

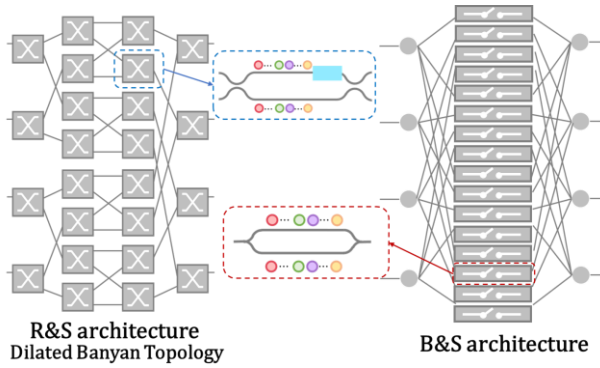


Fig. 10. Illustration of R&S and B&S architectures of switching fabric based on the RPS-MZIs.

the desired over-coupled condition. As shown in Fig. 8, when the radius (R) of the RPSs is reduced to $1.5 \mu\text{m}$, a decreases to around 0.94 due to bending loss. However, even when utilizing the pulley type coupling method and assuming perfect phase matching, the corresponding r is about 0.93 , which remains smaller than the corresponding a . As a result, achieving over-coupling in this situation is rather challenging.

To address this challenge, under-coupled RPSs stand out as a promising solution because they only require $r > a$, which eases the coupling constraints. As discussed in section 2, there are two extremums ($\pm\theta_m$) on the effective phase shift curve, corresponding to the tangent vectors OB and OC. Therefore, in a push-pull configuration, the phase change range spans from $-2\theta_m \sim +2\theta_m$. The upper limit of r can be determined by solving the simultaneous equations of the transmission circle and its tangent vector. Its expression is as follows:

$$a < r < \frac{\sqrt{2}}{2} \sqrt{\frac{a^4 k^2 + k(k - \Omega) + a^2(2 + k\Omega)}{a^2(1 + k^2)}} \quad (10)$$

where:

$$\Omega = \frac{k \tan(\theta_m)}{\sqrt{k^2 + a^4 k^2 + 2a^2(2 + k^2)}}$$

Figure 10 illustrates the upper limit of r corresponding to different θ_m in different R , suggesting that under-coupled RPSs can achieve desired phase shift for radii even less than $1.5 \mu\text{m}$.

For switching application, a phase change of π is required, so $\theta_m = \pi/4$. The corresponding transmission chart is presented by the inset in Fig. 9. When r does not equal its upper limit, there are four vectors with angles of $\pm\pi/4$ intersecting the

transmission circle (OB, OC, OE, OF). The two vectors with a larger amplitude (OB, OC) are chosen to minimize transmission loss. Contours of the transmission are depicted in Fig. 9 according to (6). As the value of r increases from the value equal to a to its upper limit, the transmission loss shows a gradual increase, ranging from approximately -3dB to around -6dB . Likewise, the single-pass phase shift ($\Delta P_{or}, \Delta P_{ob}$) and their corresponding resonance wavelength shifts ($\Delta\lambda_{or}, \Delta\lambda_{ob}$), FWHM, BW and ER can be calculated according to APPENDIX B, C, D and E.

C. Critically-coupled RPSs

As depicted in Fig. 3(b)(c), a phase singularity emerges at resonance when the RPS operates in the critical coupling regime. This spectral phase singularity, associated with zero transmission, has already been utilized in the design of perfect absorbers (PAs) in space optical metamaterials or metasurfaces[18]. This unique property can also be harnessed by the RPS as wavelength-selective absorber (WSA) in photonic circuits, particularly, for optical switches with the broadcast-and-select (B&S) architecture as shown in Fig. 10 and details are introduced in the next section.

Pairs of RPSs affiliated with the targeted absorption channels in the RPS-MZI are designed to operate in the critical coupling regime, as shown in the inset of Fig. 11(a). This configuration transforms the critically-coupled RPS-MZI into an efficient WSA, capable of achieving a narrow yet uncompromised rejection bandwidth. Supposing that ϕ under resonance conditions follow a normal distribution $N(0, \sigma^2)$, the stability of absorption can be characterized by the expected value of absorption within the range of 3σ deviation from the mean. To showcase its performance, the singly coupled critical MRR (SCC MRR)[19] is used as a reference and based on (6), we outline the contours of expected absorption difference (ΔA) of SCC MRRs over the WSA in different σ and a between SCC MRRs and the proposed WSA in Fig. 11(a). In the region of interest for parameters, all ΔA are below 0 dB , suggesting enhanced robustness of the proposed WSA. Particularly in the majority of the lower-left region, ΔA is around -3 dB , signifying a nearly twofold increase in absorption efficiency compared to SCC MRRs. With an increase of a , ΔA exhibits gradual growth, while elevating σ leads to a more pronounced increase.

In addition to its inherent stability benefits, the intentional resonance wavelength shift of the MRRs allows for the WSA to

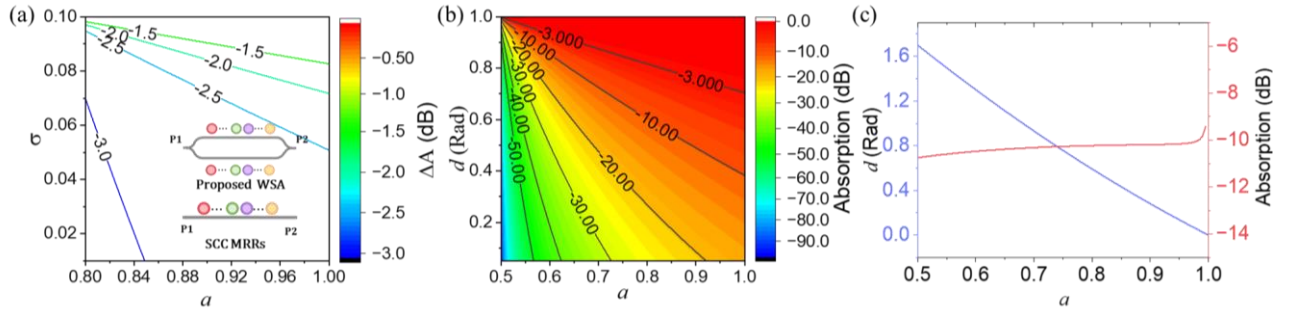


Fig. 11. (a) Contours of absorption difference (ΔA) between SCC MRRs and the proposed WSA with different standard deviations (σ) and single-pass amplitude transmission coefficient a . (b) Contour plots illustrating the absorption characteristics of the proposed WSA in different deviations d and a . (c) The critical condition for the absence of peaks within the rejection band (blue line) along with the corresponding absorption values (red line).

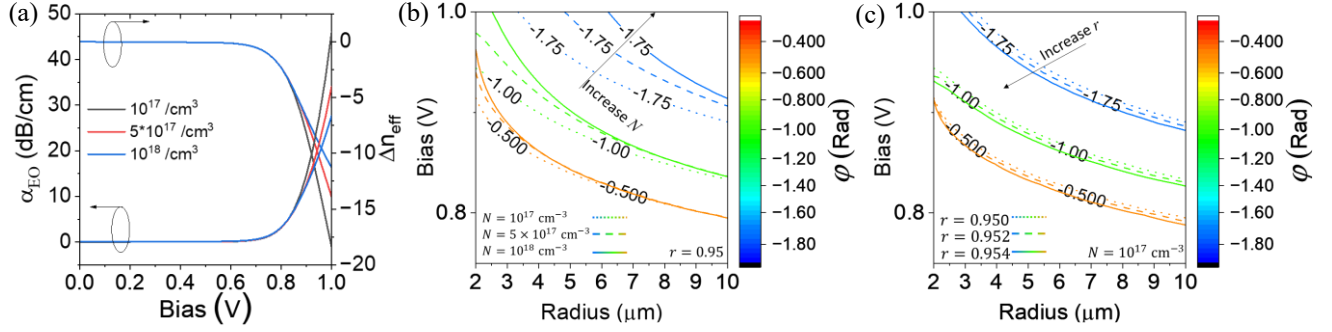


Fig. 12. (a) Power attenuation coefficient, α_{EO} and the variation in effective refractive index Δn_{eff} in different bias voltage and doping levels N . (b) Contours of effective phase shift ϕ in different bias voltages and radiuses with fixed r and increasing N . (c) Contours of effective phase shift ϕ in different bias voltages and radiuses with fixed N and increasing r .

operate in a manner that permits reconfigurability of its rejection bandwidth, while maintaining a commendable absorption efficiency. It is essential to identify the optimal tuning range for the deviation since there exists a trade-off between the rejection bandwidth and absorption efficiency. The contours of absorption in different single pass phase shift deviation d and a are given in Fig. 11(b). The region below -20 dB is deemed appropriate for absorber design as it represents the absorption of $\geq 99\%$ of the incident energy. The corresponding bandwidth at the -20 dB rejection ($BW_{-20\text{dB}}(a, r)$) can be calculated according to APPENDIX C, where $\beta = 0.01$. Sweeping d and a can find the critical condition of suppressing trough splitting, as depicted in Fig. 11(c), implying that an absorption less than -10 dB is associated with the emergence of a new peak within the stopband.

To enable multichannel absorption, within the FSR spectrum region, a certain range is intentionally reserved. When all channels need to be set to ON, the resonance wavelengths of all MRR will be set to the same center wavelength λ_{ON} within the reserved spectrum region. In addition, the overlap of all RPS resonance wavelengths significantly broadens the rejection band, consequently escalating crosstalk in adjacent channels. For the sake of simplicity in analysis, the distance between λ_{ON} and λ_N is equal to the wavelength grid spacing $\Delta\lambda$. In this situation, the FSRs of each RPS at λ_{ON} should adhere to the following condition:

$$FSR = \frac{\lambda_{ON}^2}{n_g \cdot L} \geq \Gamma + 2\Delta\lambda \quad (11)$$

Simultaneously, when all RPSs resonate at λ_{ON} , the expansion of rejection bandwidth must not compromise the ER of neighboring channels. This can be determined based on APPENDIX E and ensure favorable insertion loss is sustained across all operational states.

IV. ULTRA-DYNAMIC MULTI-DIMENSIONAL SWITCHING FABRIC

Leveraging the novel analytical tool proposed above, a multi-dimensional, ultra-dynamic switch fabric is presented with an example port count of $8 \times 8 \times 8\lambda$, presenting a general design methodology. The selection of topology plays a critical role in determining the performance of a switch fabric. Commonly utilized topologies can be divided into 2 categories: broadcast & select and route & select [20]. The B&S topology divides input data streams to all conceivable destinations and

applies selective absorption except for intended recipients. This approach becomes particularly valuable in multicast/broadcast scenarios where a solitary source necessitates simultaneous communication with numerous destinations. The classic topology of B&S architecture is illustrated in the right side of Fig. 10. It requires N^2 WSAs for an $N \times N$ switch radix. In contrast, the R&S topology accentuates network efficiency by channeling data solely to its intended endpoint. This approach affords a heightened level of control over network resources and reduces the vulnerability to congestion or superfluous data propagation. Dilated Banyan stands out as a great host to the RPS-SEs considering its complete immunity to first-order spatial crosstalk. An $N \times N$ dilated Banyan switch requires $2N(N-1)$ SEs in total [21] and high-speed drivers can be used to facilitate implementation of diverse TDM algorithms [22].

A. Circuit-level specifications break-down

The 8 wavelength channels are assigned by the Continuous-Wave Wavelength Division Multiplexing Multi-Source Agreement (CW-WDM MSA) [23]. The required FSR is approximately 9 nm minimum according to (9) so over-coupled RPSs are deemed suitable. Therefore, to achieve the overall performance of $ER_{fabric} \geq 18$ dB, $BW_{fabric} \geq 30$ GHz and $IL_{fabric} \leq 6$ dB, the corresponding performance for each SE should satisfy [24]:

$$IL_{SE} \leq \frac{IL_{fabric}}{2 \log_2 m} \quad (\text{dB})$$

$$ER_{SE} \geq ER_{fabric} + 10 \log_{10}(2 \log_2 m) - IL_{SE} \quad (12)$$

$$BW_{SE} \geq \frac{c \cdot \Delta P_{\beta}(a, r)}{\pi n_g L}$$

where IL_{SE} , ER_{SE} , BW_{SE} are the insertion loss, ER and BW for each SE. When $N=8$, 6 SE stages are used in the dilated Banyan switch, so the break-down metrics for each SE are $IL_{SE} \leq 1$ dB, $ER_{SE} \geq 25$ dB, $BW_{SE} \geq 50$ GHz.

B. Switch element design space

To attain a lower r while preserving a compact footprint, a racetrack-type RPS with a $3\mu\text{m}$ -long straight coupled waveguide is used. The injection type of E-O racetrack RPS forms by waveguides with the following parameters: W : 380 nm, H : 220 nm, H_{slab} : 62.2 nm, W_i : 0.5 μm , W_p : 1.3 μm , W_n : 1.3 μm . α_{EO} and Δn_{eff} of the waveguide under varied doping concentrations (N) and bias voltages (V) are subsequently simulated and presented in Fig. 12(a). It is observed that both

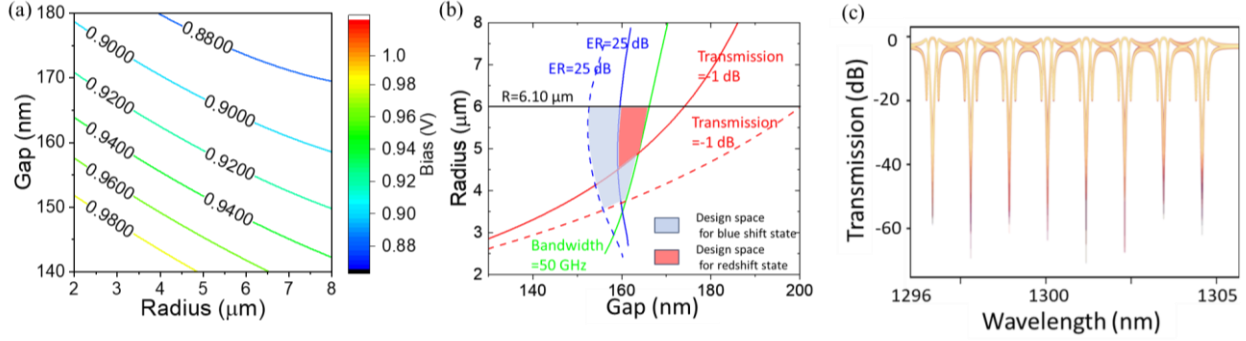


Fig. 13. (a) Contours of required bias voltage for red shift state (V_r) in different radius and gap. (b) Design space of the RPS in redshift and blueshift state. (c) Simulated transmission spectrum for all 256 switching states of our RPS-MZI switching element. The simulation is implemented by Ansys lumerical FDTD and Interconnect.

exhibit significant alterations as the bias voltage exceeds approximately 0.8V. This is the threshold voltage at which the electric field is strong enough to overcome the built-in electric field and substantially enhance the injection of carrier. The inherent resonant wavelength of the RPS is set at λ_{ib} and a bias can be applied to redshift it to λ_{ir} . Contours of $\varphi(\phi(R, V, N, r))$ for different R and V values and with changing N and r are given in Fig.12(b) and (c), respectively, according to APPENDIX B. As N , the doping concentration, increases, a higher V is required to reach the same phase at a given R . This increased voltage is necessary to counteract the built-in electric field that results from high doping levels. However, an increase in r leads to a reduction in the required V for a given R to achieve the same phase. This occurs because a larger r implies a weaker coupling strength, which results in a steeper phase change curve, thereby enhancing the efficiency of phase tuning. $N = 10^{17} \text{cm}^{-3}$ is selected as the doping concentration for efficient phase tuning.

Following APPENDIX B, a and the corresponding bias voltage for redshift (V_r) can be determined, as shown in Fig. 13(a). Since V_b and V_r has been determined, the design spaces for the RPS in redshift state and blueshift state are depicted in Fig.13(b) by finding the intersection of all required performance boundaries according to Section 3 and translate (a, r) into (Radius, Gap) according to [25]. The overlap of these two design spaces constitutes the final design space, where the requisite performance is consistently achievable, despite variations in a during the tuning process.

C. Validation through FDTD Simulations

According to the final design space outlined, we choose $R=5.5 \text{ μm}$, $G=160 \text{ nm}$, and $N = 10^{17} \text{ cm}^{-3}$ as the optimal set of parameters to construct the multi-dimensional $8 \times 8 \times 8\lambda$ switch fabric. This is also the design that we decide on running the FDTD simulations for validation. Figure 13(c) presents the simulation results for all 256 switching states of our RPS-SEs. The fourth wavelength channel exhibits the lowest ER, indicating the worst crosstalk. The simulated IL_{SE} , ER_{SE} and BW_{SE} for the fourth channel are 0.75 dB, 26.35 dB, and 53.92 GHz, respectively. A comparison with our analytical values (0.53 dB, 27.56 dB, and 56.43 GHz) reveals a good agreement with an acceptable level of error. The deviation can be attributed to the linear dispersion approximation employed in the analytical method and potential inaccuracies inherent in the FDTD simulation method. Nonetheless, it is worth noting that

all targeted metrics are consistently met, even in the worst-case scenario. This affirms the robustness of our design methodology, particularly for expedited prototyping.

V. CONCLUSION

By gaining insights into the magnitude and phase response of RPSs with an innovative compact model, we present comprehensive analyses for RPS-SEs and show its power in manipulating signal in spatial, spectral, and temporal domains. Integrating such RPSs with MZIs not only greatly enlarges its design space for efficient spectral multiplexing but also enables E-O nanosecond-scale phase tuning that was sparsely achieved with conventional add-drop MRRs. Further leveraging such a powerful analytical tool, we detail the superiority of RPS-MZIs over add-drop MRRs on metrics such as loss, extinction ratio, bandwidth, robustness and driving voltage. We also show the design robustness in under- and over-coupled regimes for wavelength routing, and in critical coupling condition for multi-band absorbing. The effectiveness of the proposed methodology is confirmed through rigorous FDTD simulations, establishing it as a potent tool for efficient and rapid prototype design and potentially making a change in the field of optical switching and signal processing.

APPENDIX A: DEPENDENCIES OF a AND φ

For precise analyses of the insertion loss in E-O RPSs, the variation of a has to be taken into consideration. Complete operating characteristics of E-O RPS can be determined by the power attenuation coefficient, $(\alpha_{EO}(N, V))$ [dB/cm], and the variation in effective refractive index $(\Delta n_{\text{eff}}(N, V))$ due to the plasma dispersion effect. Both factors are a function of the applied bias voltage (V) and the doping level (N). For the ease of analysis, the p-type and n-type doping level are assumed to be identical. Considering both carrier injection and curvature of waveguide, a can be expressed as:

$$a(R, V, N) = a_{\text{bend}} \alpha_{EO} \quad (\text{A1})$$

where:

$$a_{\text{bend}} = 10^{-\left(\frac{\alpha_{\text{bend}}}{20}\right) \frac{2\pi R}{10000}}$$

$$\alpha_{EO} = 10^{-\left(\frac{\alpha_{EO}}{20}\right) \frac{(2\pi R + 2Lc)}{10000}}$$

The power attenuation coefficient due to waveguide curvature, denoted as α_{bend} [dB/cm], correlates with the radius

of waveguide curvature (R) and adheres to a power law relationship [12]. The effective phase shift can be given by:

$$\varphi(\phi(R, V, N)) = \varphi\left((2\pi R + 2Lc) \frac{2\pi}{\lambda_i} \Delta n_{\text{eff}}(N, V) + \phi_0\right) \quad (\text{A2})$$

where ϕ_0 is the single pass phase shift when no bias voltage is applied. (A1) and (A2) imply that a can be expressed as a function of ϕ , providing insight into how a changes with varying values of ϕ . After conducting simulation and fitting, we establish the relationship between a and ϕ : $a(\phi) = -0.06676(\phi + \phi_0)^2 + 0.02446(\phi + \phi_0) + 0.9942$ under a specific design parameters: W : 380 nm, H : 220 nm, H_{slab} : 62.2 nm, W_i : 0.5 μm , W_p : 1.3 μm , W_n : 1.3 μm , N : $10^{17} / \text{cm}^3$. The transmission circle charts are given in Fig. 4(b) according to (5) and $a(\phi)$ with $\phi_0 = 0.15$, clearly depicting the distortion and contraction under the influence of plasma dispersion effect.

APPENDIX B: POWER TRANSMISSION FOR BAR AND CROSS STATE

Assuming that light is injected into P1 of MZI, power transmission coefficients for P3 and P4 can be given, respectively, by:

$$T_3(\varphi_u, \varphi_l, |t_u|, |t_l|) = \frac{|t_u|^2}{4} + \frac{|t_l|^2}{4} - \frac{|t_u||t_l|}{2} \cos(\varphi_u - \varphi_l) \quad (\text{B1})$$

$$T_4(\varphi_u, \varphi_l, |t_u|, |t_l|) = \frac{|t_u|^2}{4} + \frac{|t_l|^2}{4} + \frac{|t_u||t_l|}{2} \cos(\varphi_u - \varphi_l) \quad (\text{B2})$$

where $|t_u|$ ($|t_l|$) and φ_u (φ_l) are the optical field amplitude transmission coefficient and the corresponding phase on the upper arm (lower arm), respectively. For T-O transmission circle, as shown in the inset of Fig. 6(a), the power transmission of single RPS can be calculated by simple geometry:

$$\begin{aligned} |t_u|^2 &= |t_l|^2 = |OB|^2 = |OC|^2 \\ &= \frac{1}{2} \left(\frac{r - a^2 r}{1 - a^2 r^2} \right. \\ &\quad \left. + \sqrt{\frac{-2a^2 r^2 + 2a^2 - r^2 + 2a^2 r^4 - a^4 r^2}{(1 - a^2 r^2)^2}} \right)^2 \end{aligned} \quad (\text{B3})$$

By substituting (B3) and the corresponding phases into (B1), we have:

$$\begin{aligned} T_{\text{cross}} = T_{\text{bar}} &= \frac{(|OB| + |OC|)^2}{4} = |OB|^2 = |OC|^2 \\ &= \frac{1}{2} \left(\frac{r - a^2 r}{1 - a^2 r^2} \right. \\ &\quad \left. + \sqrt{\frac{-2a^2 r^2 + 2a^2 - r^2 + 2a^2 r^4 - a^4 r^2}{(1 - a^2 r^2)^2}} \right)^2 \end{aligned} \quad (\text{B4})$$

By solving (B4) and (3) simultaneously, the single-pass phase shifts (ΔP_{0r} , ΔP_{0b}) and their corresponding resonance wavelength shifts ($\Delta \lambda_{0r}$, $\Delta \lambda_{0b}$), with a $\pi/2$ phase bias, can be given, respectively, as:

$$\begin{aligned} \Delta P_{0r} &= -\Delta P_{0b} \\ &= \arccos \left(\frac{-a^2(a^2 + 3)r^3 + 3a^2 r + r + (a^4 r^4 - 1)\Psi}{2a(-a^2 r^4 + 1 + (a^2 r^3 - r)\Psi)} \right) \end{aligned} \quad (\text{B5})$$

$$\begin{aligned} \Delta \lambda_{0r} &= -\Delta \lambda_{0b} \\ &= \text{FSR} \cdot \frac{P_{0r}}{2\pi} = \frac{\lambda_0^2}{2\pi n_g L} \Delta P_{0r} \end{aligned} \quad (\text{B6})$$

where:

$$\Psi = \sqrt{\frac{2a^2 r^4 - (a^2 + 1)^2 r^2 + 2a^2}{(a^2 r^2 - 1)^2}}$$

For E-O transmission circle, (B3), (B4), (B5), and (B6) persist in their validity. However, a crucial adjustment is required: replace the a with a distinct value for the calculation of $|OB|$ and $|OC|$, which corresponds to the $3\pi/4$ and $-3\pi/4$ phase shifts. For a given RPS, The effective phase shift can be given by:

$$\begin{aligned} \varphi(\phi(R, V, N, r)) &= \varphi\left((2\pi R + 2Lc) \frac{2\pi}{\lambda_i} \Delta n_{\text{eff}}(N, V \right. \\ &\quad \left. - V_b) + \Delta P_{0b}(a(R, V_b, N), r)\right) \end{aligned} \quad (\text{B7})$$

where V_b is the applied bias when RPS in blueshift state and can be deliberately predetermined. The applied bias for the redshifts (V_r) can be obtained by letting (B7) equal $-7\pi/4$. Since we have already obtained V_b and V_r , a corresponding to the $3\pi/4$ and $-3\pi/4$ phase shifts can be determined according to (A1). Consequently, $|OB|$ and $|OC|$ can be determined by substitute $a(R, V_b, N)$ and $a(R, V_r, N)$ into (B3) respectively. Then the power transmission of T_{bar} and T_{cross} can be given by (6).

APPENDIX C: 3DB BANDWIDTH AND FWHM

As shown in Fig. 5(c), the passband of the RPS-SEs displays a maximum at the operating wavelength λ_i with the peak value equal to T_{bar} and the RPS i and RPS i' operating at distances of $\Delta \lambda_{ir}$ and $\Delta \lambda_{ib}$ away from λ_i . The deviation of the operating wavelength from λ_i will lead to the decrease of transmission according to (B1) and (B2). When the power transmission declines, we have:

$$\begin{aligned} T_3(\varphi(\Delta P_{0r} + \Delta P_{\beta}), \varphi(\Delta P_{0b} + \Delta P_{\beta}), |t_{MRR}(\Delta P_{0r} \\ + \Delta P_{\beta})|, |t_{MRR}(\Delta P_{0b} + \Delta P_{\beta})|) \\ = \beta \cdot T_{\text{bar}} \end{aligned} \quad (\text{C1})$$

where ΔP_{β} is the additional single pass phase shift caused by the operating wavelength deviating from λ_i . ΔP_{β} can be obtained by solving (1) (B1), (B5) and (C1) simultaneously. When $\beta=1/2$, ΔP_{β} corresponds to the FWHM and it can be fitted with a quadric surface as follows:

$$\begin{aligned} \Delta P(a, r) &= p_{00} + p_{10}r + p_{01}a + p_{20}r^2 + p_{11}ra \\ &\quad + p_{02}a^2 \end{aligned} \quad (\text{C2})$$

where p_{00} , p_{10} , p_{01} , p_{20} , p_{11} and p_{02} are 3.118, -10.01, 7.175, -1.323, 10.03 and -8.997, respectively. Under the assumption of linear dispersion approximation, the FWHM and BW can be given by (7) and (8). When m the RPS-SEs cascade, the BW and FWHM of the whole system can be obtained by let $\beta = (\frac{1}{2})^{1/m}$.

APPENDIX D: TRANSMISSION DETERIORATION DUE TO FINITE VOLTAGE RESOLUTION

Assume the single pass phase shift error due to finite voltage resolution is $\delta\phi$ ($\delta\phi > 0$). The increase of $\delta\phi$, will lead to the deterioration of insertion loss and extinction ratio according to (B1) and (B2). The single pass phase shift tuning resolution (ϕ_{res}) meeting a specific ER requirement is characterized by the range of values for $\delta\phi$ that fulfill the ER criteria. Further multi-physics simulation can be conducted based on the specific geometry and doping level to give the voltage produce a ϕ_{res} single pass phase shift. This voltage is exactly the minimum driving voltage resolution.

APPENDIX E: DERIVATION OF EXTINCTION RATIO

If we define the unbalanced ratio (α) for the two arms of MZI as:

$$\alpha = \frac{|t_u|}{|t_b|} \quad (E1)$$

Then ER can be expressed as:

$$ER(\alpha, \Delta\phi) = \frac{T_3}{T_4} = 1 - \frac{4 \cos(\Delta\phi)}{\alpha + \frac{1}{\alpha} + 2 \cos(\Delta\phi)} \quad (E2)$$

Therefore, the ER for channel i ($ER_i(\alpha_i, \Delta\phi_i)$) under crosstalk from all the other channels can be given by:

$$ER_i(\alpha_i, \Delta\phi_i) = \left(1 - \frac{4 \cos(\Delta\phi_i)}{\alpha_i + \frac{1}{\alpha_i} + 2 \cos(\Delta\phi_i)}\right) \cdot T_{bar} \quad (E3)$$

where:

$$\Delta\phi_i = \sum_{i \neq k}^{M-1} (\varphi(\Delta P_{kb} + \Delta S_k) - \varphi(\Delta P_{kr} + \Delta S_k)) + \pi$$

$$\alpha_i = \prod_{i \neq k}^{M-1} \frac{|t_{MRR}(\Delta P_{kb} + \Delta S_k)|}{|t_{MRR}(\Delta P_{kr} + \Delta S_k)|} \quad (E4)$$

$$\Delta P_{kb} = \Delta P_{kr} = 2\pi \cdot \Delta\lambda_{kr} / \text{FSR}$$

Here, M is the total number of channels. ΔP_{kb} and ΔP_{kr} are the single pass phase shift of the k -th pair of RPSs corresponding to the redshift wavelength $\Delta\lambda_{kr}$, blueshift wavelength $\Delta\lambda_{kb}$. ΔS_k is the single pass phase shift of the k -th pair of MRPSs when operating wavelength deviating from λ_k to λ_i .

REFERENCES

- [1] M. D. Feuer, D. C. Kilper, and S. L. Woodward, "ROADMs and their system applications," in *Optical Fiber Telecommunications V B (Fifth Edition)*, I. P. Kamniov, T. Li, and A. E. Willner, Eds., in *Optics and Photonics*, Burlington: Academic Press, 2008, pp. 293–343.
- [2] J. Kundrát, O. Havliš, J. Jedlinský, and J. Vojtěch, "Opening up ROADMs: Let Us Build a Disaggregated Open Optical Line System," *J. Lightwave Technol.*, *JLT*, vol. 37, no. 16, pp. 4041–4051, Aug. 2019.
- [3] Y. Li, J. Lin, L. Zong, S. K. Bose, B. Mukherjee, and G. Shen, "Colorless, partially directionless, and contentionless architecture for high-degree ROADMs," *J. Opt. Commun. Netw., JOCN*, vol. 14, no. 6, pp. 481–492, Jun. 2022.
- [4] T. J. Seok et al., "MEMS-Actuated 8×8 Silicon Photonic Wavelength-Selective Switches with 8 Wavelength Channels," in 2018 Conference on Lasers and Electro-Optics (CLEO), May 2018, pp. 1–2.
- [5] M. Stepanovsky, "A Comparative Review of MEMS-Based Optical Cross-Connects for All-Optical Networks From the Past to the Present Day," *IEEE Communications Surveys & Tutorials*, vol. 21, no. 3, pp. 2928–2946, 2018.
- [6] K. Biswas and A. Sarkar, "MEMS-based Optical Switches," in *Optical Switching*, John Wiley & Sons, Ltd, 2022, pp. 93–106.
- [7] A. Rizzo et al., "Massively scalable Kerr comb-driven silicon photonic link," *Nat. Photon.*, Jun. 2023, doi: 10.1038/s41566-023-01244-7.
- [8] A. Farhadi-Beldachi, E. Huques-Satas, A. Tzanakaki, Y. Yan, R. Nejabati, and D. Simeonidou, "Experimental Demonstration of 5G Fronthaul and Backhaul Convergence Based on FPGA-Based Active Optical Transport," in 2018 European Conference on Optical Communication (ECOC), Rome: IEEE, Sep. 2018, pp. 1–3.
- [9] Q. Cheng, M. Bahadori, M. Glick, and K. Bergman, "Scalable Space-And-Wavelength Selective Switch Architecture Using Microring Resonators," in 2019 Conference on Lasers and Electro-Optics (CLEO), May 2019, pp. 1–2.
- [10] R. Stabile, A. Rohit, and K. A. Williams, "Monolithically Integrated 8 × 8 Space and Wavelength Selective Cross-Connect," *Journal of Lightwave Technology*, vol. 32, no. 2, pp. 201–207, Jan. 2014.
- [11] B. G. Lee and N. Dupuis, "Silicon Photonic Switch Fabrics: Technology and Architecture," *Journal of Lightwave Technology*, vol. 37, no. 1, pp. 6–20, Jan. 2019.
- [12] A. S. P. Khope et al., "Multi-wavelength selective crossbar switch," *Opt. Express*, vol. 27, no. 4, p. 5203, Feb. 2019.
- [13] L. Y. Dai, V. Gopal, and K. Bergman, "Ultra-scalable Microring-based Architecture for Spatial-and-Wavelength Selective Switching," in 2023 IEEE Silicon Photonics Conference (SiPhotonics), Apr. 2023, pp. 1–2.
- [14] L. Lu, L. Zhou, X. Li, and J. Chen, "Low-power 2×2 silicon electro-optic switches based on double-ring assisted Mach-Zehnder interferometers," *Opt. Lett.*, vol. 39, no. 6, p. 1633, Mar. 2014.
- [15] L. Lu et al., "4×4 Silicon Optical Switches Based on Double-Ring-Assisted Mach-Zehnder Interferometers," *IEEE Photon. Technol. Lett.*, vol. 27, no. 23, pp. 2457–2460, Dec. 2015.
- [16] Z. Guo, L. Lu, L. Zhou, L. Shen, and J. Chen, "16 × 16 Silicon Optical Switch Based on Dual-Ring-Assisted Mach-Zehnder Interferometers," *Journal of Lightwave Technology*, vol. 36, no. 2, pp. 225–232, 2018.
- [17] W. Bogaerts et al., "Silicon microring resonators," *Laser & Photon. Rev.*, vol. 6, no. 1, pp. 47–73, Jan. 2012.
- [18] M. Liu et al., "Spectral phase singularity and topological behavior in perfect absorption," *Phys. Rev. B*, vol. 107, no. 24, p. L241403, Jun. 2023.
- [19] E. Sanchez-Cristobal et al., "Integrated microring resonator as a perfect absorber," in *Frontiers in Optics 2015 (2015)*, paper JW2A.21, Optica Publishing Group, Oct. 2015, p. JW2A.21.
- [20] Q. Cheng, M. Bahadori, Y.-H. Hung, Y. Huang, N. Abrams, and K. Bergman, "Scalable Microring-Based Silicon Clos Switch Fabric With Switch-and-Select Stages," *IEEE Journal of Selected Topics in Quantum Electronics*, vol. 25, no. 5, pp. 1–11, Sep. 2019.
- [21] Q. Cheng et al., "Silicon Photonic Switch Topologies and Routing Strategies for Disaggregated Data Centers," *IEEE J Sel Top Quant*, vol. 26, no. 2, pp. 1–10, Mar. 2020.
- [22] H. Chung, H. H. Lee, K. O. Kim, K.-H. Doo, Y. Ra, and C. Park, "TDM-PON-Based Optical Access Network for Tactile Internet, 5G, and Beyond," *IEEE Network*, vol. 36, no. 2, pp. 76–81, Mar. 2022.
- [23] "CW-WDM MSA: Defining laser standards for AI, HPC and high-density optics," CW-WDM MSA. Accessed: Dec. 13, 2023. [Online]. Available: <https://cw-wdm.org/>
- [24] T. S. El-Bawab, Ed., *Optical switching*. New York ; London: Springer, 2005.
- [25] M. Bahadori et al., "Design Space Exploration of Microring Resonators in Silicon Photonic Interconnects: Impact of the Ring Curvature," *J. Lightwave Technol.*, vol. 36, no. 13, pp. 2767–2782, Jul. 2018.